Magnetism and anomalous transport in the Weyl semimetal PrAlGe: Possible route to axial gauge fields: Supplementary Information

Daniel Destraz[1*], Lakshmi Das[1], Stepan S. Tsirkin[1], Y. Xu[1], Titus Neupert[1], J. Chang[1*], A. Schilling[1], Adolfo G. Grushin[2], Joachim Kohlbrecher[3], L. Keller[3], Pascal Puphal[4], Ekaterina Pomjakushina[4] and Jonathan S. White[3*]

[1]*Physik-Institut, Universität Zürich, Winterthurerstrasse 190, CH-8057 Zürich, Switzerland*

[2]*Univ. Grenoble Alpes, CNRS, Grenoble INP, Institut Neel, 38000, Grenoble, France*

[3]*Laboratory for Neutron Scattering and Imaging (LNS), Paul Scherrer Institute (PSI), CH-5232 Villigen, Switzerland*

[4]*Laboratory for Multiscale Materials Experiments (LMX), Paul Scherrer Institut (PSI), CH-5232 Villigen PSI, Switzerland*

* To whom correspondence should be addressed. E-mail: destraz@physik.uzh.ch, johan.chang@physik.uzh.ch, jonathan.white@psi.ch

Supplementary Note 1

Time-dependent bulk magnetic and transport data Here we explore further the magnetic properties of PrAlGe below T_c by bulk magnetic and electrical transport. Supplementary Fig. 1 shows time (t-)dependent magnetization and Hall resistivity data obtained at $B = 0$. For these measurements a magnetic field above saturation along c was applied upon cooling and subsequently removed when at the desired measurement temperature, followed by the measurements recorded over an extended period. Time-dependent data were recorded after field-cooling to temperatures both above and below T_g.

At 2 K < T_g, Supplementary Fig. 1a reveals both magnetization and Hall resistivity to be finite at $t = 0$, with their concomitant decay indicating the slow, yet spontaneous, reversal of Pr moments aligned with the original direction of $\mu_0 H$ during the FC. This shows a spontaneous relaxation of the bulk magnetization, with the observed decay described by the sum of a stretched exponential and a constant term

$$m(t) = m_{\mathrm{A}} exp\left(-\left(\frac{t}{\tau}\right)^{\beta}\right) + m_{\infty}. \tag{S1}$$

The data at 2 K are shown in Supplementary Fig. 1a. The values of $\tau = 0.7$ h and $\beta = 0.2$ are in the typical range for spin glasses [1-4].

Upon increase in temperature above T_g, the effect vanishes. At 12 K > T_g, Supplementary Fig. 1b shows completely reversible behaviour on the time-scale of our measurements, and no residual magnetization or Hall resistivity even at $t = 0$.

Supplementary Note 2

Seebeck effect In Supplementary Fig. 2 we show Seebeck effect isotherms for different magnetic fields. The data reveal an extremely weak low magnetic field dependence. At high temperatures the Seebeck signal is positive, indicating positive charge carriers, consistent with the Hall effect measurements. The signal crosses zero at 14 K and becomes negative for lower temperatures.

Supplementary Note 3

Quantitative comparison between anomalous transport in PrAlGe and other systems

The size of the AHE in PrAlGe can be compared with other relevant magnetic materials by plotting the anomalous Hall angle $\Theta_H^A = \rho_{xy}^A / \rho_{xx}$ against either σ_{xy}^A (as done for Fig. 5 of Ref. 5) or the anomalous Hall factor $S_H = \sigma_{xy}^A/M$ (as done for Fig. 5 of Ref. 6). In Supplementary Fig. 3 the values of $\Theta_H^A = 3.7\%$, $\sigma_{xy}^A = -367\ \Omega^{-1}\mathrm{cm}^{-1}$, and $S_H = 0.087\ \mathrm{V}^{-1}$ for PrAlGe are plotted along with those of other values reported in the literature, and are seen to lie well within the general range of values seen for other compounds. A similar comparison can be made with the size of the extrapolated anomalous Nernst signal $N^A \approx 28$ nV / K, which lies as well within the general range of values expected for FM metals when plotted against the saturation magnetization [7], as shown in Supplementary Fig. 3c.

Supplementary Note 4

Analysis and interpretation of SANS profiles SANS intensity distributions like those observed from PrAlGe in Fig. 2 of the main text qualitatively resemble those observed from magnetic systems known to display inhomogeneous magnetization densities, such as spin glasses [9] and random anisotropy magnets [10]. In many of these systems the intensity versus $|q|$ profiles can be modelled analytically by combinations of Lorentzian and Lorentzian-squared lineshapes centered at $q = 0$ [9,11-14]. This simple model fails to describe our data for two reasons. First, it does not describe the evolution of a T-dependent length scale in the system that is manifested as a point of largest curvature in the SANS profiles [see Fig. 2e of the main text]. Second, due to this T-dependent length scale, the model cannot describe the q-scaling of the intensity which is characterized by a change in slope of the high-q ($|q| > 0.02$ Å^{-1}) portion of the data.

In the following, we describe a minimal model for the SANS intensity profiles based on a smoothly varying radial profile of the spatial variation in scattering contrast, viz. moment orientation [15,16]. According to the model, the distance over which the scattering amplitude varies corresponds to a characteristic length scale that is manifested in the SANS profiles, while the radial form of the scattering-contrast over this length scale yields the form of the q-scaling at high-q. Here we use a slightly adapted version of a model introduced by Boucher *et al.* [15] that describes a spherically-symmetric radial scattering length density profile. In our case, we assume a similarly parameterized, yet cylindrically symmetric magnetisation profile. By assuming a cylindrical geometry instead of a spherical one, we take into account the easy-axis magnetic anisotropy of PrAlGe. The z-component of the magnetisation vector is modelled to follow the profile given by Boucher:

$$M_z(r,R,\alpha) = |M| \begin{cases} \left(1-\left(\frac{r}{R}\right)^2\right)^{\frac{\alpha}{2}-2} & r \leq R \\ 0 & r > R \end{cases} \tag{S2}$$

Here $|M|$ parameterises the magnetisation vector at the origin $r = 0$, R is the radius of cylindrical cross-section over which the contrast varies, and α describes the radial-dependence profile. According to this parameterization, the variation of M_z with R originates from a tilting into the detector plane of an otherwise constant modulus of the magnetisation vector $|M|$. This can be realized in different ways. Two possibilities are shown in Supplementary Fig. 4. In the top row, the case for radially-tilted magnetic moments are shown, while in the bottom row a model of in-plane tilted magnetic moments is shown.

To calculate final scattering intensities, we follow the magnetic scattering formalism presented in Ref. 17, and calculate the form factor for both spin-flip and non spin-flip scattering channels. The calculation of the different scattering contributions show that the model of radially-tilted spins will not give any spin-flip contribution, whereas the model of in-plane curled magnetic moments does. Therefore, we apply the simpler radially-tilted spins model for fitting our data obtained with unpolarised neutrons, but note that SANS experiments using a full polarisation analysis will allow a distinction to be made between the two above-described models. Nevertheless, both models describe scattering in the non spin-flip channel that has the same functional dependency and can be calculated via the Fourier transform of the z-component of the Halpern-Johnson vector [17,18], which in our case is identical to the z-component of the magnetisation profile. The scattering amplitude is thus given by

$$F(q,R,\alpha) = \int_0^R M_z(r,R,\alpha) 2\pi r L J_0(qr) dr \tag{S3}$$

where J_0 is a zeroth order Bessel function of the first kind, and L describes the cylinder length. Since the cylindrical axis is defined to be parallel to the neutron beam, the value of L does not contribute to the observed $|q|$-dependence of the intensity, and it is absorbed as a scaling factor. The parameter α determines the potential law at large q-value in the scattering pattern $\lim_{q\to\infty} I(q) \propto q^{-\alpha}$. Furthermore we assume a distribution of cylinder radii for our objects so that the scattering intensity is averaged over a size distribution $N(R,R_m,\sigma)$

$$I(q) = \int_0^\infty N(R,R_m,\sigma) F^2(q,R,\alpha)\, dR. \tag{S4}$$

Here $N(R,R_m,\sigma)$ describes a log-normal distribution, with mean radius R_m and width σ. Finally, the overall model includes a further polynomial function to account for background non-magnetic scattering from the crystal and the sample environment, and which is assumed to be temperature independent.

A global fit of the model to all datasets is included in Fig. 2e of the main text. From the fitting parameters α and R_m, we obtain information regarding the particle surface properties and length scale, respectively. Supplementary Fig. 5a shows α increases monotonically as the temperature falls, from ~5 close to T_c, to ~7 at the lowest temperatures. These values of α are in reasonable agreement with the range α = (4+2β), where $0 < \beta < 1$ describes a so-called `smooth pore boundary' for which the scattering strength varies more smoothly over the distance R by the power β [15,16].

While α is observed to increase with decreasing T, Supplementary Fig. 5b shows R_m instead to generally fall with decreasing T, from $R_m \sim 25$ nm close to T_c, to ~14 nm by base T. This fall of R_m indicates a narrowing of the characteristic distance over which the scattering strength varies due to the magnetic structure across the cylindrical surface. Notably, the variation of R_m slows down far below T_g (which in zero field lies in the vicinity of T_c [19]), and α evolves smoothly over the entire T range. These results imply a freezing of the magnetic inhomogeneity length-scale and motion by ~ 6 K deep in the glass-like regime, while the topology of the magnetization variation at the particle surface evolves over the entire T range. To understand the weak sensitivity of the magnetic inhomogeneity properties to the spin-glass transition, further studies are in progress that include direct imaging studies of the nanoscale magnetic texture by magnetic force microscopy measurements.

Finally, in Supplementary Fig. 6 we present a further visualization for clarifying the origin of the magnetic SANS signal. First, Supplementary Fig. 6a shows the real-space variation (normal to the cylindrical axis) of $M_z/|M|$ for values of α according to Eq. S2. Corresponding depictions in three dimensions for the radially-tilted moment model are shown in Supplementary Figs. 6b-d for various α. Here the arrows indicate the variation in local magnetization that yields a variation in $M_z/|M|$ consistent with Eq. S2. Thus according to Eq. S2, α = 4 describes the radial profile of a cylinder with homogeneous scattering amplitude. For the magnetic case, this corresponds to a magnetization aligned along z that is uniform across the cylinder plane, and describes so-called Porod scattering from `smooth surfaces', or wrinkle-free and sharp domain walls in the context of magnetic systems. For PrAlGe, larger α values are needed to describe the scattering below T_c, thus describing a smoother decrease of $M_z/|M|$ with increasing r. This is achieved by introducing the tilting of the magnetization away from the easy-axis as visualized in Supplementary Figs. 6c and d.

Supplementary Note 5

Band Structure and Berry Curvature Supplementary Figure 7a shows the calculated band structure of PrAlGe along the high symmetry directions, which is essentially the same as reported previously [20]. To visualize the contributions of different parts of momentum space to the anomalous Nernst effect, we note that in the low temperature limit, Eq. 3 in the main text reduces to a Fermi-surface integral:

$$\alpha_{xy} = \frac{\pi^2}{3}\frac{k_B^2 T}{e}\frac{\partial \sigma_{xy}}{\partial \mu}\bigg|_{E_F} \propto -\oint\!\!\oint_{FS} dS \frac{\Omega_z}{v_F} \tag{S5}$$

In Supplementary Figure 7b we show the Fermi surface of PrAlGe colored by the magnitude of Ω_z/v_F. One can see that there are spots of high magnitude, both positive and negative, which are located near the Weyl points close to the Fermi level.

As mentioned in the main text, large Berry curvature may also arise from avoided crossings that arise generally in the band structure. To demonstrate this in Supplementary Figure 7c we plot the Berry curvature in the $k_x = 0$ plane. One can see that a ring of rather large (both positive and negative) Berry curvature arises from the avoided crossing of two bands of opposite spin that would be exactly degenerate in the absence of spin-orbit coupling (SOC). SOC breaks this degeneracy, leaving only discrete Weyl points. However, there is no strict way of separating the contribution of the gapped degeneracy line to the anomalous transport from the contribution due to Weyl nodes, because to some extent the former may be considered as a tail of the latter. We also note that in Supplementary Figure 7c the Berry curvature around the Weyl points near the line $k_y a/2\pi$~0.25 appears small because the associated nodes are far from the $k_x = 0$ plane compared to those along $k_y a/2\pi$~0.46. That can also be seen easily from main text Figure 5a.

Supplementary References

References

1 Anand, V.K. et al. Magnetic and transport properties of $Pr_2Pt_3Si_5$. *Journal of Magnetism and Magnetic Materials* **324**, 2483-2487 (2012)

2 Anand, V.K., Adroja, D.T. & Hillier A.D. Ferromagnetic cluster spin-glass behavior in $PrRhSn_3$. *Phys. Rev. B* **85**, 014418 (2012)

3 Mitcheler, P.D., Roshko, R.M. & Ruan, W. Non-equilibrium relaxation dynamics in the spin glass and ferromagnetic phases of CrFe. *Philisophical Magazine* **68**, 539-550 (1993)

4 Campbell, I.A. Critical exponents of spin-glass systems. *Phys. Rev. B* **37**, 9800-9801 (1988)

5 Liu, E *et al.* Giant anomalous Hall effect in a ferromagnetic kagome-lattice semimetal. *Nat. Phys.* **14**, 1125-1131 (2018).

6 Kim, K. *et al*. Large anomalous Hall current induced by topological nodal lines in a ferromagnetic van der Waals semimetal. *Nat. Mater.* **17**, 794-799 (2018).

7 Yang, H. *et al*., Giant anomalous Nernst effect in the magnetic Weyl semimetal $Co_3Sn_2S_2$.

Preprint at https://arxiv.org/abs/1811.03485 (2018)

8 Guin, S.N. *et al.* Anomalous Nernst effect beyond the magnetization scaling relation in the ferromagnetic Heusler compound Co2MnGa. NPG Asia Materials. 11, 16 (2019).

9 Hicks, T.J. Magnetism in disorder. *Oxford, Clarendon* (1995)

10 Michels, A. & Weissmüller, J. Magnetic-field-dependent small-angle neutron scattering on random anisotropy ferromagnets. *Rep. Prog. Phys.* **71**, 066501 (2008)

11 Kogon, H.S. & Wallace, D.J. The Ising model in a random field; supersymmetric surface fluctuations and their implications in three dimensions. *J. Phys. A: Math. Gen.* **14**, L527-L531 (1981)

12 Birgeneau, R.J., Yoshizawa, H., Cowley, R.A., Shirane, G. & Ikeda, H. Random-field effects in the diluted two-dimensional Ising antiferromagnet $Rb_2Co_{0.7}Mg_{0.3}F_4$. *Phys. Rev. B* **28**, 1438-1448 (1983)

13 Mirebeau, I., Lequien, S., Hennion, M., Hippert, F. & Murani, A.P. Small angle neutron scattering in reentrant spin glasses. *Physica B* **156-157**, 201-204 (1989)

14 Piatek, J.O. *et al.*, Nonequilibrium hysteresis and spin relaxation in the mixed-anisotropy dipolar-coupled spin-glass $LiHo_{0.5}Er_{0.5}F_4$. *Phys. Rev. B* **90**, 174427 (2014)

15 Boucher, B., Chieux, P., Convert, P. & Tournarie, M. Small-angle neutron scattering determination of medium and long range order in the amorphous metallic alloy $TbCu_{3.54}$. *J. of Phys. F: Metal Physics* **13**, 1339-1357 (1983)

16 Schmidt, P.W. Modern aspects of small-angle scattering. *Kluwer Academic* (1995)

17 Mühlbauer, S. *et al.*, Magnetic small-angle neutron scattering. *Rev. Mod. Phys.* **91**, 015004 (2019)

18 Halpern, O. & Johnson, M.H. On the magnetic scattering of neutrons. *Phys. Rev.* **55**, 898-923 (1939)

19 Puphal, P. *et al.* Bulk single-crystal growth of the theoretically predicted magnetic Weyl semimetals *R*AlGe (*R* = Pr, Ce). *Phys. Rev. Materials* **3**, 024204 (2019)

20 Chang, G. et al. Magnetic and noncentrosymmetric Weyl fermion semimetals in the *R*AlGe family of compounds (*R* = rare earth). *Phys. Rev. B* **97**, 041104 (2018).

Supplementary Figures

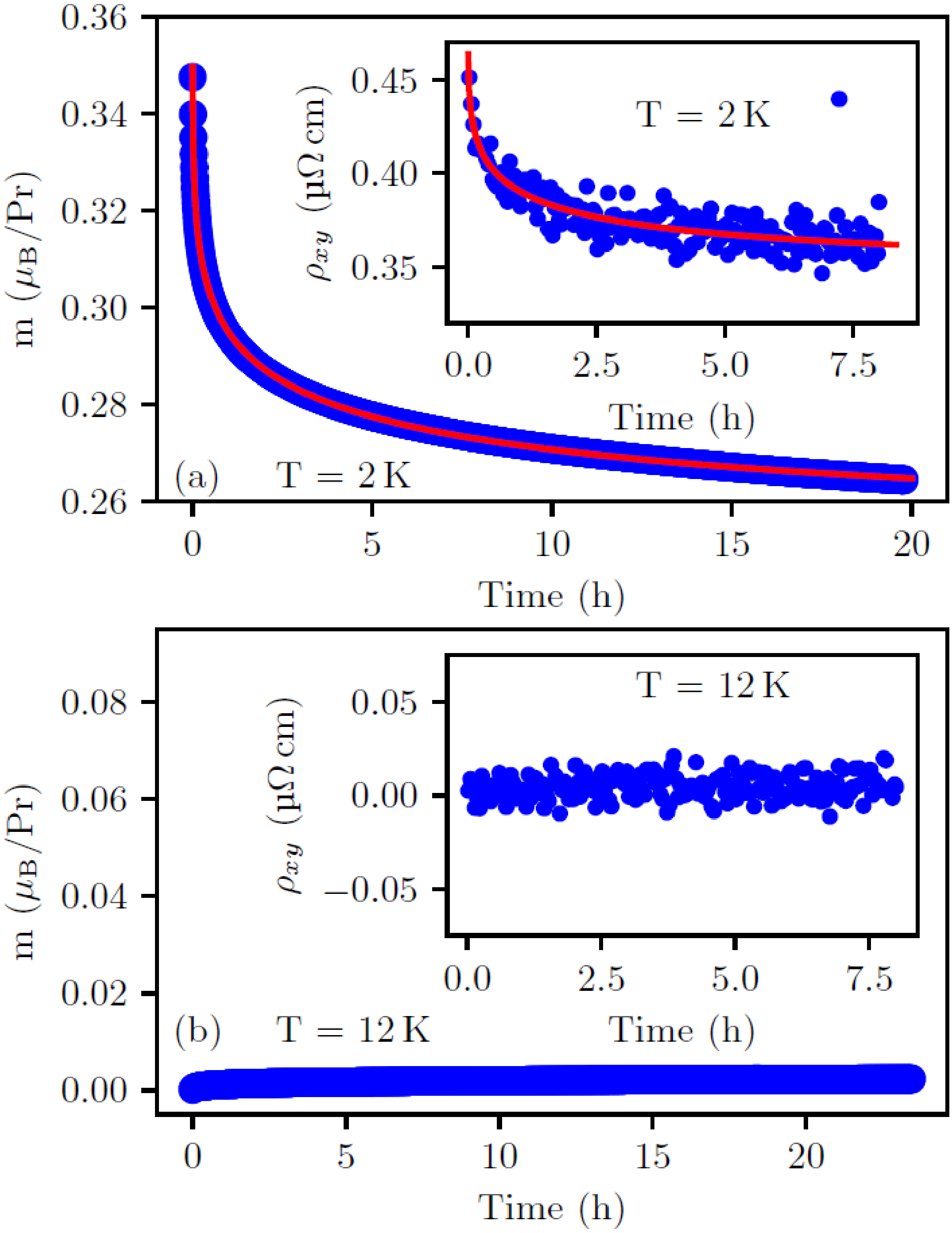

Supplementary Figure 1 | Time-dependent magnetization and Hall resistivity. The magnetization (main panel) and the Hall resistivity (inset) as a function of time after cooling in a field above the saturation field and subsequently setting the field to zero, for **a** $T = 2$ K and **b** $T = 12$ K. The red line in **a** are fits to Eq. S1.

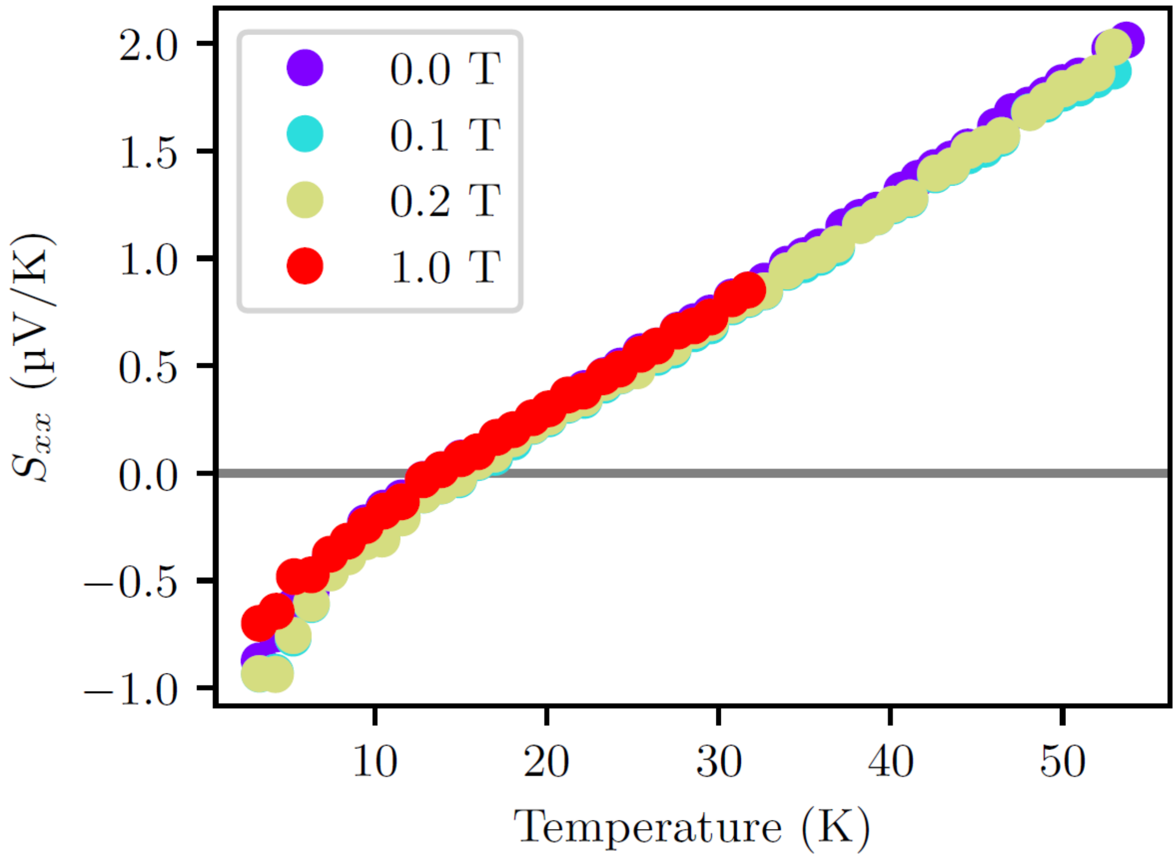

Supplementary Figure 2 │ Seebeck effect. Seebeck effect in PrAlGe, where zero is crossed at ≈ 14 K for each magnetic field.

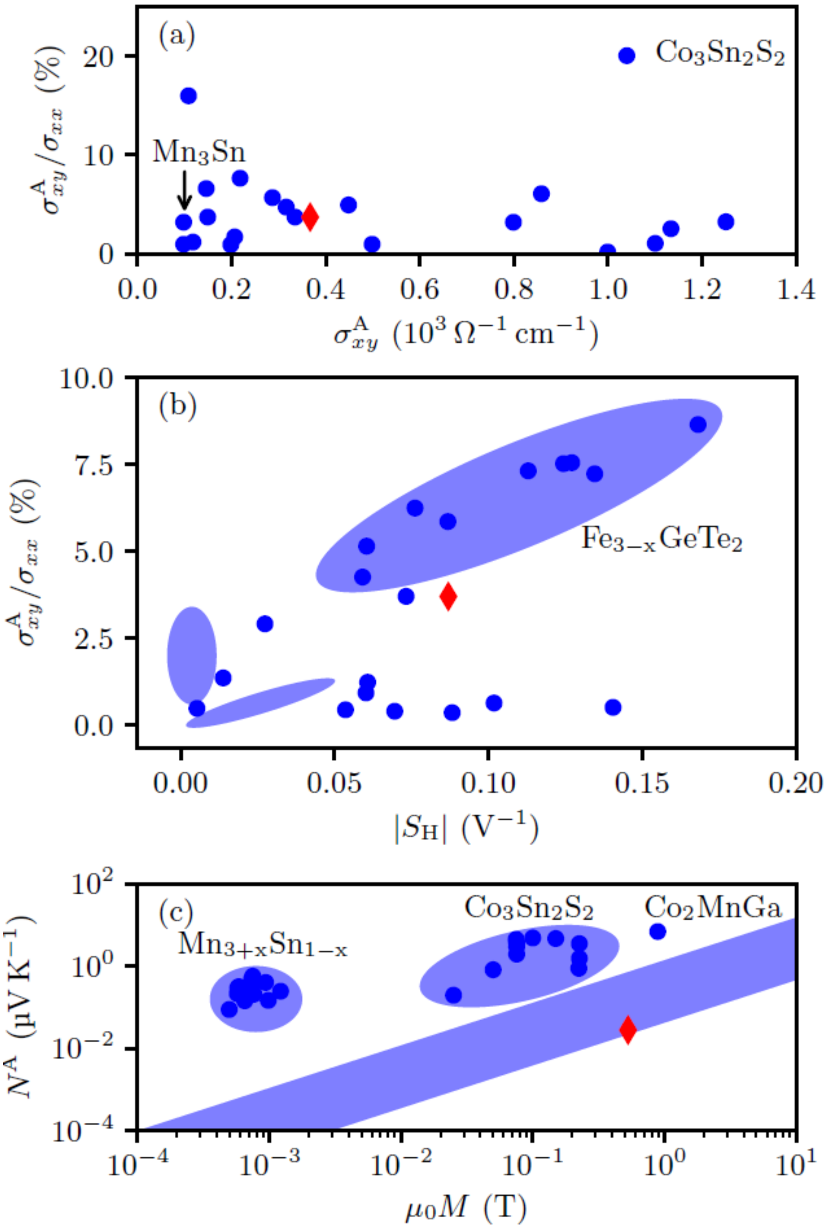

Supplementary Figure 3 | Literature comparison. Anomalous Hall angle σ_{xy}^{A} / σ_{xx} in PrAlGe versus **a** anomalous Hall conductivity, **b** anomalous Hall factor. **c** shows the anomalous Nernst signal versus magnetization. Red diamonds indicates the results of the present study. Blue symbols denote values reported for other materials in the literature and are taken from Ref. 5 for panel **a**, from Ref. 6 for panel **b** and from Refs. 7 and 8 for panel **c**. The blue ellipses in panel **b** indicate substitution systems. The blue band in panel **c** covers the range of many FM metals.

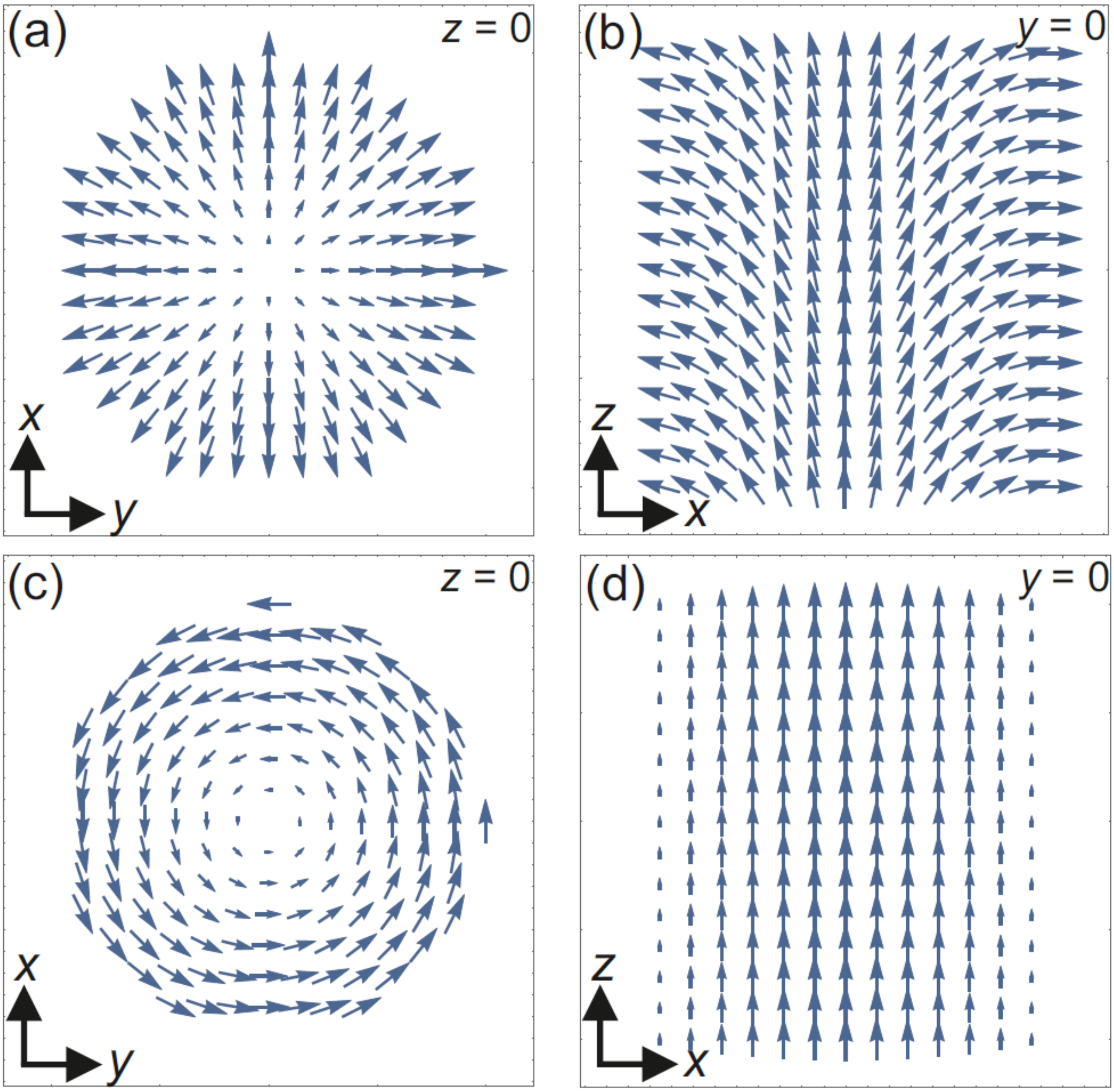

Supplementary Figure 4 │ Cross-sections of magnetization profiles Cuts through magnetization profiles in the *xy*-plane (detector plane) and the *xz*-plane. Arrows denote the direction of the local magnetization vector. Panels **a** and **b** are for the radially-tilted moment model, while **c** and **d** are for the in-plane curled magnetic moment model

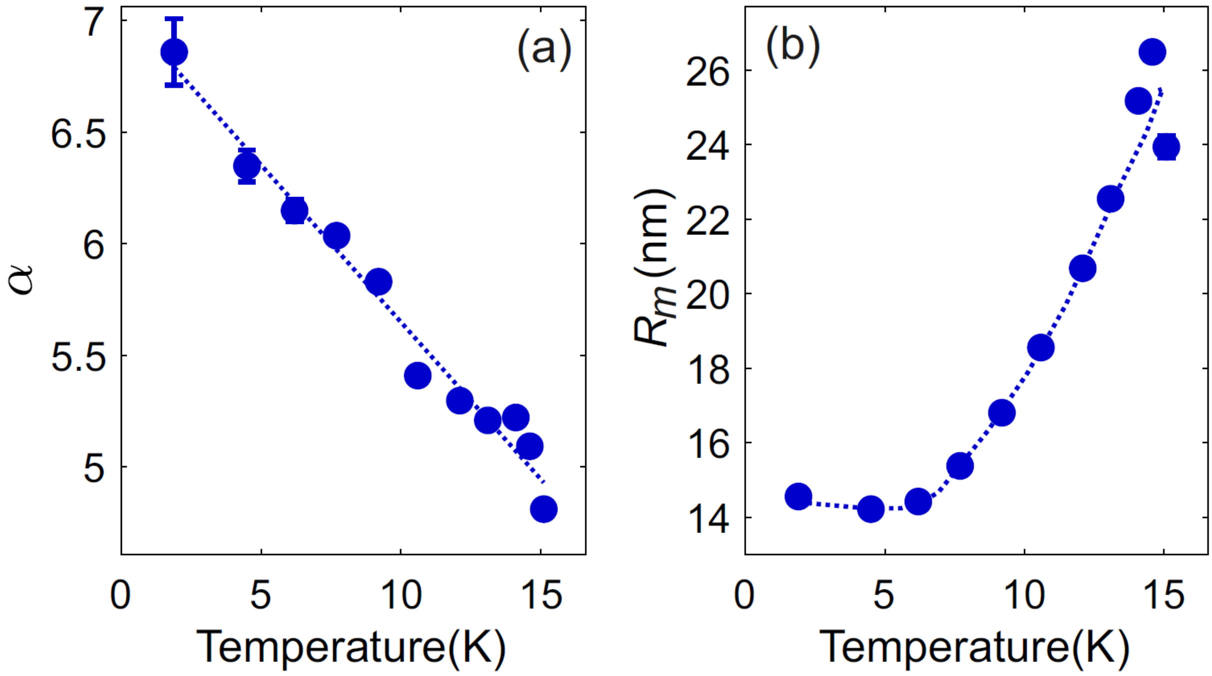

Supplementary Figure 5 │ Parameters obtained from model fitting of the SANS data. T-warming dependence at $\mu_0 H = 0$ after ZFC for the fitted parameters **a** α and **b** R_m for the fits of the model that are shown in Fig. 2e of the main text. In each panel, dashed lines are guides for the eye. Where visible, error bars indicate the standard error.

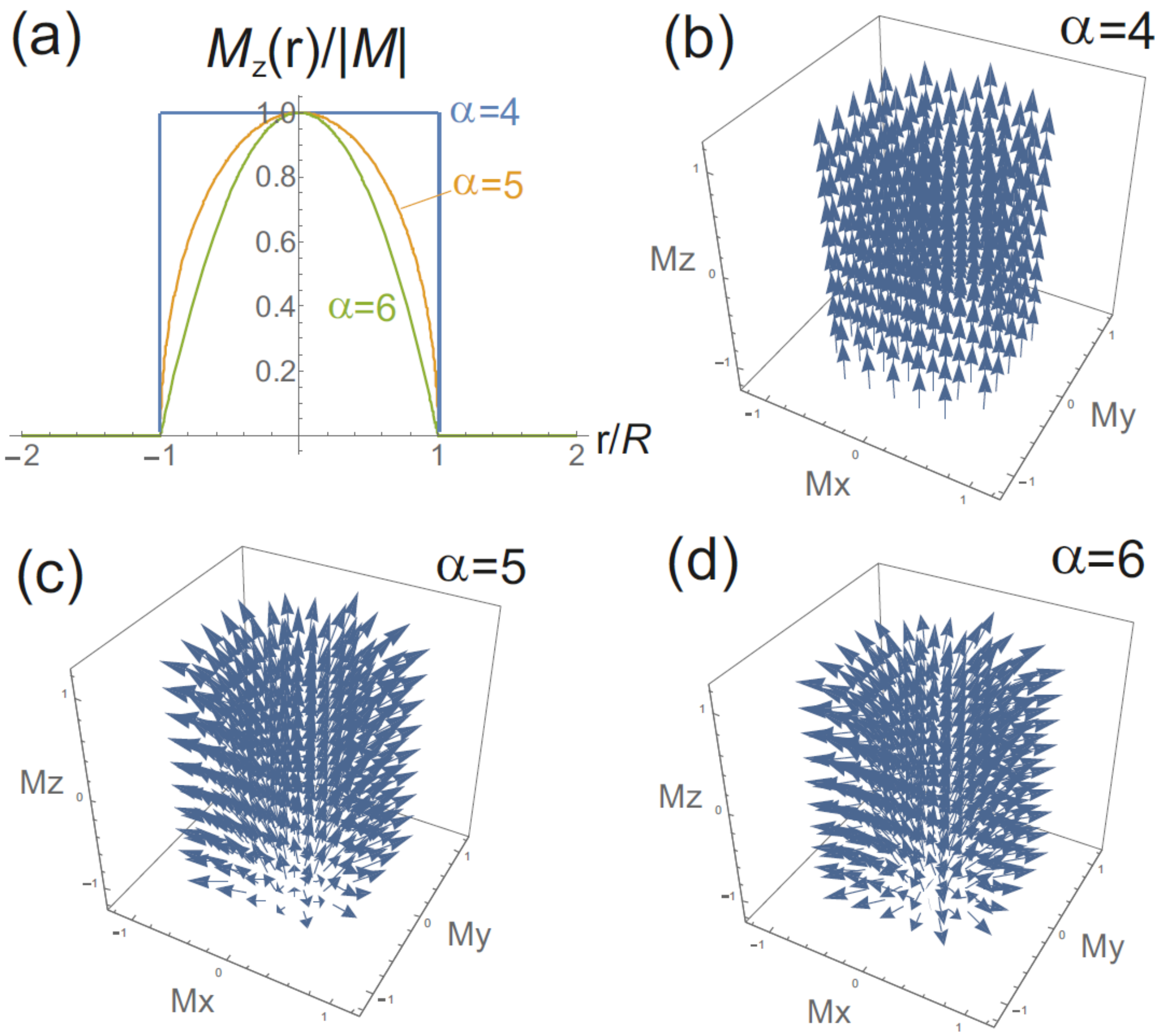

Supplementary Figure 6 │ Radial-dependence of magnetic contrast. a Radial profiles in one-dimension of the z-component of the normalized magnetization for various α according to Eq. S2. Panels **b** - **d** show the possible representation due to a three-dimensional spherically-symmetric radial profile for **b** $\alpha = 4$, **c** $\alpha = 5$, and **d** $\alpha = 6$. Arrow symbols are included to indicate the possible spatial variation of the magnetization. In panels **b-d**, all three dimensions are normalized to the nominal cylinder size of radius R and length L.

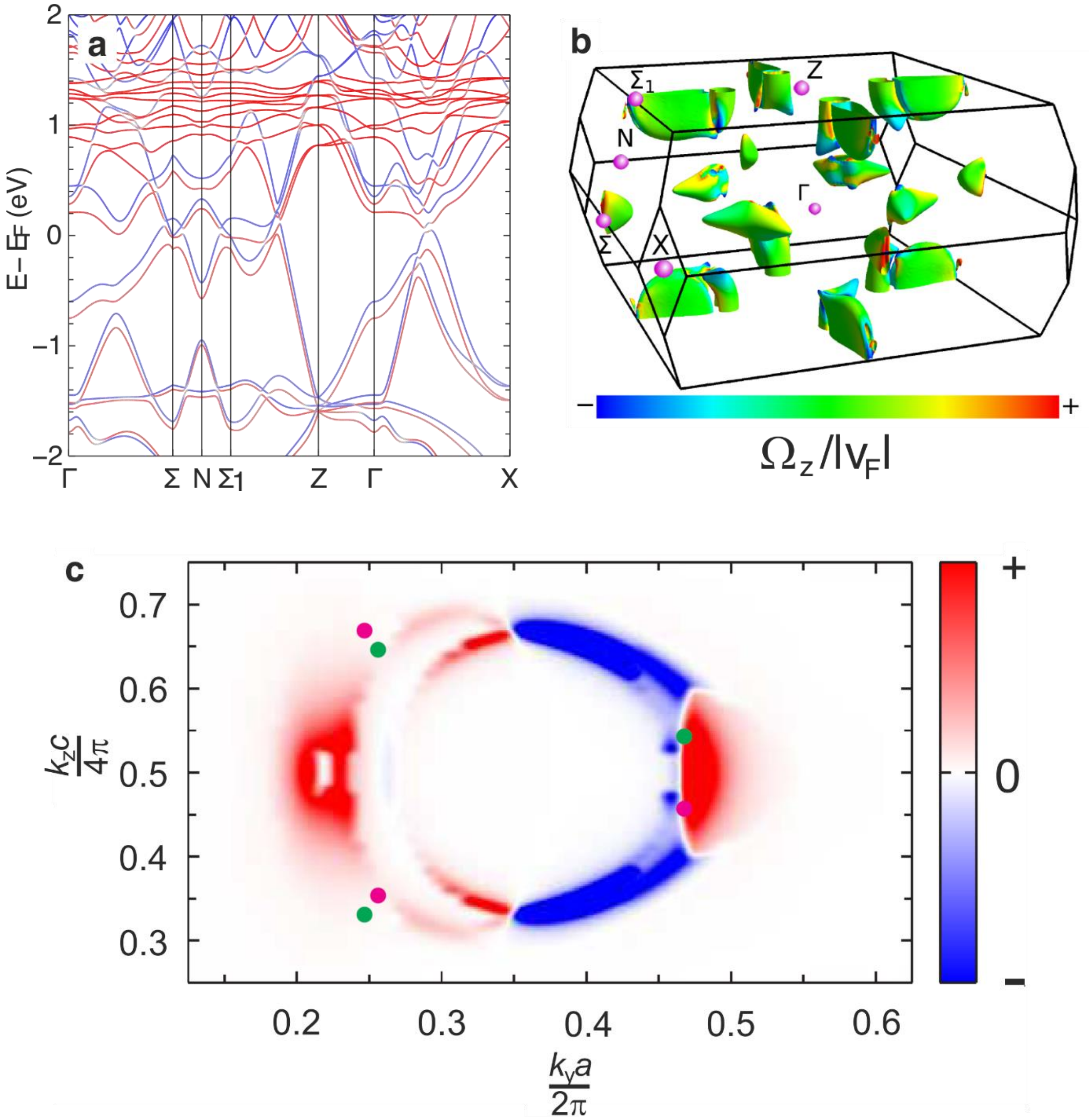

Supplementary Figure 7 │ Fermi surface of PrAlGe and Berry curvature in presence of ferromagnetic *order*. a Calculated band structure for PrAlGe along high symmetry directions. The color shows the expectation value of the *z* component of the spin operator, with red (blue) corresponding to positive (negative) values. **b** The calculated Fermi surface for the whole Brillouin zone. The color scaling indicates the size of $\Omega_z/|v_F|$, where a logarithmic transformation has been used for large absolute values. Red color corresponds to positive Berry curvature while blue corresponds to negative Berry curvature. Magenta spheres indicate high symmetry points. **c** Negative Berry curvature Ω_z (summed over states below the Fermi level) in the plane $k_x = 0$, with red (blue) corresponding to positive (negative) values. Green (magenta) dots indicate projections of Wey points of positive (negative) chirality, located in the vicinity of the $k_x = 0$ plane. See main text Figure 5a for more details.